

Deep-learning-assisted inverse design of dual-spin/frequency metasurface for quad-channel off-axis vortices multiplexing

Kai Qu¹, Ke Chen¹,* Qi Hu, Junming Zhao, Tian Jiang, and Yijun Feng*

Nanjing University, School of Electronic Science and Engineering, Nanjing, China

Abstract. Recently, the metasurfaces for independently controlling the wavefront and amplitude of two orthogonal circularly polarized electromagnetic (EM) waves have been demonstrated to open a way toward spin-multiplexing compact metadevices. However, these metasurfaces are mostly restricted to a single operation frequency band. The main challenge to achieving multiple frequency manipulations stems from the complicated and time-consuming design caused by multifrequency cross talk. To solve this problem, we propose a deep-learning-assisted inverse design method for designing a dual-spin/frequency metasurface with flexible multiplexing of off-axis vortices. By analyzing the cross talk between different spin/frequency channels based on the deep-learning method, we established the internal mapping relationship between the physical parameters of a meta-atom and its phase responses in multichannels, realizing the rapid inverse design of the spin/frequency multiplexing EM device. As a proof of concept, we demonstrated in the microwave region a dual-frequency arbitrary spin-to-orbit angular momentum converter, a dual-frequency off-axis vector vortex multiplexer, and a large-capacity (16-channel) vortex beam generator. The proposed method may provide a compact and efficient platform for the multiplexing of vortices, which may further stimulate their applications in wireless communication and quantum information science.

Keywords: metasurface; deep learning; frequency multiplexing; spin-decoupled; optical vortex.

Received Nov. 28, 2022; accepted for publication Dec. 9, 2022; published online Jan. 5, 2023.

© The Authors. Published by SPIE and CLP under a Creative Commons Attribution 4.0 International License. Distribution or reproduction of this work in whole or in part requires full attribution of the original publication, including its DOI.

[DOI: [10.1117/1.APN.2.1.016010](https://doi.org/10.1117/1.APN.2.1.016010)]

1 Introduction

The angular momentum carried by light can be specifically divided into two types of spin angular momentum (SAM) and orbital angular momentum (OAM).¹ The SAM described by $\sigma\hbar$ per photon (topological charge $\sigma = \pm 1$) is related to the polarization state of light waves, whereas the OAM described as $l\hbar$ leads to the “doughnut” intensity distribution and helical phase wavefront of light, where topological charge l is an integer and ϕ is the azimuth angle. In recent decades, due to the orthogonality of the transmission between different OAM modes and their peculiar wavefronts, multiple OAM beams can be encoded with different information at the same time to tremendously increase the channel capacity in optical/wireless communication;^{2–6} thus the beam carrying OAM (or termed

a vortex beam, VB) has attracted great research interest and triggered numerous potential applications in wireless communication,^{4–6} optical holography,^{7,8} and quantum information processing.⁹ Moreover, if two vortex beams carrying OAM with opposite spin states propagate along the same direction, they will be superimposed coherently to form a vector vortex beam (VVB) with an inhomogeneous state of polarization wavefront,¹ which plays a pivotal role in optical tweezers,^{10,11} spin-Hall photonics,^{12–15} and spin object detection,^{16,17} etc.¹⁸ Nevertheless, classical devices for VB and VVB generation, including spiral phase plates, spiral and twisted reflectors, diffraction gratings, and circular phased arrays, suffer from their high profile and bulky configuration, limited mode number, etc.^{19,20}

The emergence of metasurfaces not only realizes some peculiar physical phenomena,^{21–25} but also effectively solves the problem of bulky devices.²³ In general terms, although metasurfaces based on the Pancharatnam–Berry (PB) phase^{26,27} (or so-called geometric phase) have tackled the problem of high

*Address all correspondence to Ke Chen, ke.chen@nju.edu.cn; Yijun Feng, yjfeng@nju.edu.cn

profile, they still have limitations on the realization of topological charge and direction of generated off-axis vortices.^{24,28,29} The linear-polarization-multiplexing metasurface can be realized by designing structures with anisotropic form,^{30,31} but it is difficult to realize the multiplexing of circular polarization. Fortunately, an emerging avenue in metasurface design to unlock two spin states is proposed by combining both geometric phase and propagation phase, which affords a promising platform for de-linked spin multiplexing of electromagnetic (EM) functionalities,³² such as arbitrary spin-to-OAM conversion^{24,28} and spin-decoupled beam shaping.^{33,34} However, it is still challenging to enable arbitrary and high-efficiency spin-to-OAM conversion in multiple frequency bands because the frequency/spin cross talk will increase the complexity of structure configuration.³⁵ More importantly, such cross talk will largely increase the time-cost in the design and optimization, making it hard or extremely time-consuming to solve the cross talk problem manually (see detailed discussion in Section S1 in the [Supplementary Material](#)).

In the past few years, typical methods of deep learning (e.g., neural networks) have been developed to solve complex EM problems and conceive metasurface-based devices.^{36–39} The main principle is to use a black box to fit the relationship between input and output parameters.³⁹ The data that can characterize the desired EM performance are taken as input, while the variables that can change the EM response of the meta-atom are taken as output,³⁶ such as physical parameters^{40–51} and feed voltage.^{52–54} This on-demand design method can accelerate the design process of metasurfaces, saving much time spent in optimization, reducing the threshold of designer's professional knowledge, and thus has been used for designing various meta-devices, such as absorbers,⁵⁵ chiral mirrors,⁴⁰ beam-steering devices,⁵⁶ plasmonic metasurfaces,⁵⁷ holographic imaging,⁵² and invisibility cloaks.⁵³ Notably, when deep learning is applied to directly establish the connection between input and output, it will take much time to generate a large number of samples in order to support the training process if there is no existing data set. Fortunately, the combination of prior knowledge and deep-learning methodology can make inverse design more purposeful, thereby largely reducing the time spent on generating training samples.^{58–60} However, most of the existing studies are only for one polarization channel or a single-frequency band, leaving much potential for larger channel capacity unexploited.

Herein, we develop a deep-learning-assisted method to achieve inverse design of dual-spin and dual-frequency metasurfaces capable of providing independent wavefront tailoring in multiple information channels. A deep-learning-assisted method, including classifier, multilayer perceptron (MLP, a kind of classic artificial neural network, ANN), and prior-knowledge-guided adaptive optimization are applied to obtain the inverse design of every meta-atom required in the metadvice. Once the required wavefront of each channel is determined, the physical parameters of each meta-atom of the metasurface can be output without human interference, freeing people from the tedious and time-consuming process of optimizing parameters manually. As the proof of concept, quad-channel VBs carrying independent OAM and dual-frequency off-axis VVB generation are experimentally demonstrated in the microwave region. The proposed metasurface provides a pivotal degree of freedom of frequency/wavelength in addition to the conventional spin-decoupled method,³² and further expands the channel capacity relative to the spectrally interleaved geometric phase

metasurfaces,⁶¹ which may bring potential innovation to the improvement of channel capability in wireless/optical communication.

2 Results

2.1 Inverse Design of the Dual-Spin/Frequency Meta-Atom

Figure 1 shows the schematic of the dual-spin/frequency multiplexing metasurface. When a pair of orthogonal circularly polarized (CP) planar waves with two different frequencies illuminating onto the metasurface-based VB generator, different OAM modes are produced independently in four distinct channels, e.g., with topological charge of $l = +2, +1, -1, \text{ and } -2$. The spin states of the incident and reflected light wave are consistent, showing a spin-locked characteristic.^{62,63} More importantly, these four reflective channels are isolated well due to the inverse design and adaptive optimization of elements by the deep-learning-assisted method. It can automatically output physical parameters of all the meta-atoms required in the target metasurface with the desired wavefront for the quad channels. Compared with other traditional methods, this strategy can reduce the design time cost while increasing the number of circular polarization multiplexing channels and effectively avoiding the tedious manual parameter optimization process.

The wavefront output by the spatially varying metasurface element determines the scattering pattern of the entire metasurface, for which the design of the meta-atom with corresponding phase modulation capability is necessary. Combining both the geometric phase and the propagation phase is an effective method to independently control the wavefront of a pair of orthogonal CP waves.³² Assuming that α is the rotation angle of the meta-atom, φ^R and φ^L are the phase shifts of the meta-atom under the illumination of right-circularly polarized (RCP) and left-circularly polarized (LCP) waves, respectively. For a meta-atom containing both the propagation phase and geometric phase, the orientation angle α and the propagation phase responses for a linearly polarized (LP) wave can be calculated as²⁸

$$\alpha = (\varphi^R - \varphi^L)/4, \quad (1)$$

$$\varphi^x = (\varphi^R + \varphi^L)/2, \quad (2)$$

$$\varphi^y = (\varphi^R + \varphi^L)/2 - \pi, \quad (3)$$

where φ^x and φ^y are the copolarized phase shifts for the LP waves, and they should satisfy the condition of $\varphi^x - \varphi^y = \pi$.³² For an arbitrary combination of φ^R and φ^L , one just needs to calculate φ^x , φ^y and α according to Eqs. (1)–(3). It can be used to predict the phase behavior of a single-band spin-decoupled metasurface well, as it is easy to design an anisotropic metasurface operating for a dual-LP wave with very low polarization cross talk.^{28,34} As for designing a dual-band spin-decoupled metasurface, the ideal condition requires that the reflection amplitude be unitary and that there is no phase cross talk between high-frequency channels and low-frequency ones. Unfortunately, such an ideal condition is difficult to construct for two closely adjacent frequency bands³⁵ because the simultaneous change of the rotation angle and the physical parameters of the resonator will bring much unpredictable cross talk among two frequency

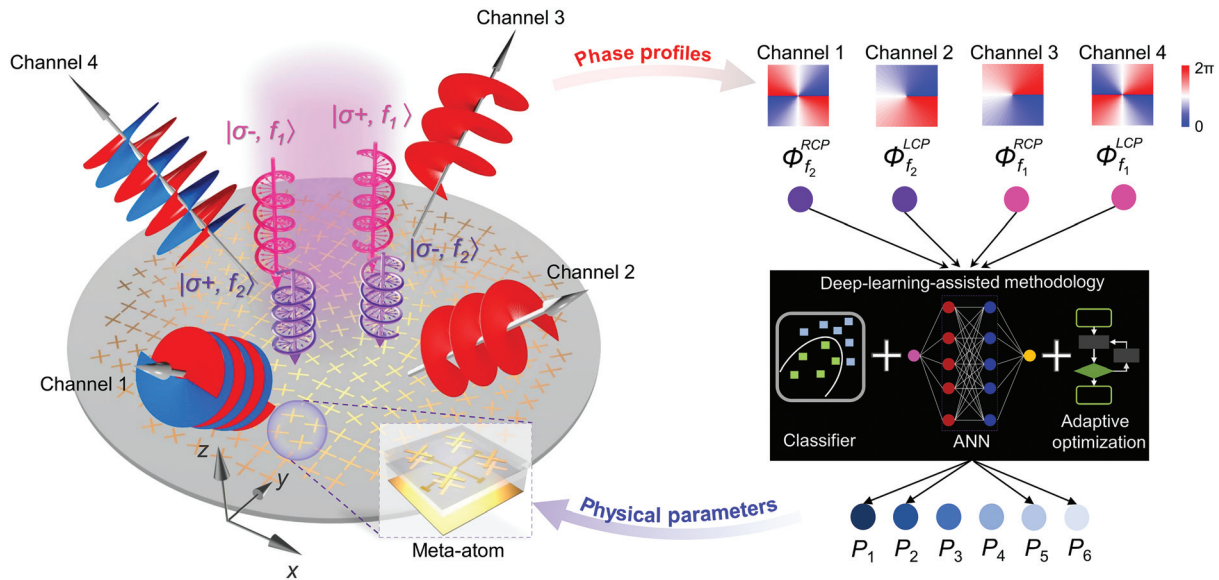


Fig. 1 Conceptual schematic of the dual-spin/frequency multiplexing metasurface for spin-to-OAM conversion and its inverse design approach. Light with opposite spin states and different frequencies converted to optic vortex carrying arbitrary OAM mode after being reflected from the metasurface. The inset shows the spiral phase distribution of the four VBs with topological charges $l = +2, +1, -1, -2$. When the wavefronts for quadruplex channels are input to the deep-learning-assisted methodology, physical parameters for all the meta-atoms of the metasurface can be automatically output without human interference. $\{P_1, P_2, P_3, P_4, P_5, P_6\}$ are the physical parameters of the meta-atom mainly determining its EM responses in quadruplex channels.

and two spin polarization channels, especially in the microwave region, where the dual-band meta-atoms are mostly constructed by metallic/dielectric layers. The irregularity of cross talk makes it a huge challenge to quickly and systematically design dual-frequency spin-decoupled metasurfaces with a thin thickness. Besides, although by adding frequency-selective structures or air spacer could alleviate the cross talk, these methods inevitably increase the overall thickness of the metasurfaces.^{64–66}

To accelerate the design process and free us from performing some tedious and time-consuming optimization tasks, here we use the deep-learning method to realize the fast classification of phase modulation requirements and the propagation phase prediction under the influence of cross talk, making spin and frequency multiplexing technology easier and more convenient. If the high- and low-frequency resonant structures are designed in the same layer, they are easy to touch or cross with each other when both of them need to be rotated and stretched, which will completely destroy the EM response of the meta-atom. Based on this consideration, we use a multilayer structure to form the dual-frequency and dual-spin metasurface. Actually, a conventional way to adopt a neural network in metasurface community is to divide the metallic or dielectric resonant pattern into deep-subwavelength pixels,^{42,45,46,55} but these patterns usually only have a single layer, considering the calculation complexity. However, such methods are impossible for both spin- and frequency-multiplexing operations, as multilayered metasurface structures are used; otherwise, the time cost of calculation will be unpredictable. To speed up and simplify the design process, in the first step, we employ the popular cross-shaped resonators and roughly design a multilayered meta-atom operating in a dual-frequency band supporting both geometric phase and

propagation phase in the dual band. The multilayer configuration, as shown in Fig. 2(a), has the potential to verify the principle of quad-channel wavefront control. The meta-atom consists of four copper layers with a thickness of 0.018 mm and three dielectric layers (Taconic TRF-43). The dielectric spacers are fixed and have the thicknesses of $h_1 = 1$ mm, $h_2 = 1$ mm, and $h_3 = 1.63$ mm with relative permittivity of 4.3 and loss tangent of 0.0033, respectively. Four cross-shaped metallic patterns of equal size are used as the top and middle metallic layers, which determine the EM response at high frequency. Particularly, this double-layer setup improves the coverage of the high-frequency propagation phase when these cross-shaped metallic patterns stretch (see Section S2 in the [Supplementary Material](#) for more details). The third metallic layer is composed of Jerusalem-cross pattern that mainly provides a low-frequency response. Parameters α and β , respectively, represent the rotation angle of the large and small cross-shaped resonators with respect to the y axis, which is used to provide the required geometric phase in two frequency bands. The lengths of the metallic arms of the Jerusalem-cross pattern in the x and y directions are denoted as l_{x1} and l_{y1} , respectively. Similarly, l_{x2} and l_{y2} are used to characterize the size of the small cross-shaped resonators in the top and middle metallic layers. Other dimensions are $p = 10$ mm, $a = 0.4$ mm, $b = 0.3$ mm, and $w = 1$ mm. When α and β are fixed as 0 deg, the reflection propagation phases can cover almost 360 deg in two frequency bands from 9.6 to 10 GHz and 17.6 to 18 GHz for both x - and y -polarized incidence by tuning the parameters of l_{x1} , l_{y1} , l_{x2} , and l_{y2} .

When the meta-atom operates at low frequency, both geometric phase and propagation phase will suffer from the cross talk

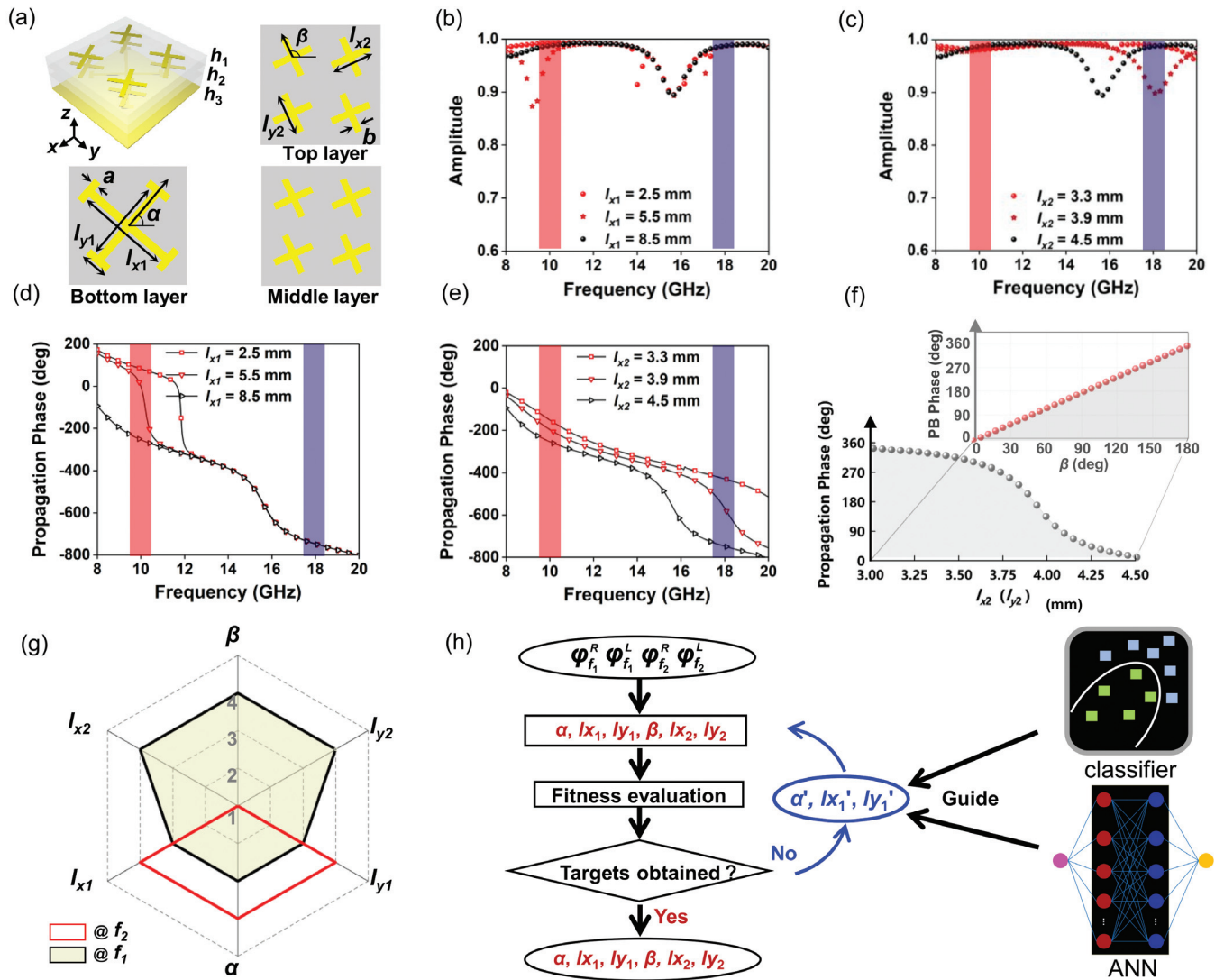


Fig. 2 EM response of the meta-atom and realization of the inverse design. (a) Schematic of the meta-atom with multilayer configuration. The geometric parameters of the top layer and middle one are the same. When rotation angles of all the cross resonators remain 0 deg, the simulated linearly copolarized amplitude under x -LP illumination with (b) only l_{x1} varying from 2.5 to 8.5 mm or (c) only l_{x2} varying from 3.3 to 4.5 mm. (d) and (e) The simulated phase spectra corresponding to (b) and (c), respectively. In particular, parameters $\{l_{y1}, l_{x2}, l_{y2}\}$ are fixed at $\{6$ mm, 4.5 mm, 3.3 mm $\}$ when l_{x1} varies, and parameters $\{l_{y2}, l_{x1}, l_{y1}\}$ are fixed at $\{4.5$ mm, 8 mm, 6 mm $\}$ when l_{x2} varies. (f) At high frequency, simulated geometric phase response with the rotation angle β varying from -90 deg to 90 deg and the propagation phase response with different dimensions l_{x2} at 17.8 GHz. The parameters l_{y2} , l_{x1} , and l_{y1} are fixed at 4.5, 8, and 6 mm, respectively. Actually, the changes in these three parameters hardly affect the propagation phase for x -LP at high frequency. For the geometric phase curve at high frequency, the fixed values of l_{x1} and l_{y1} are the same as above, and l_{x2} , l_{y2} are fixed to 4.5 and 3.93 mm, aiming to ensure a phase difference of 180 deg between two orthogonal LP waves. (g) Influence of six parameters on wavefront modulation in the dual frequency. (h) Flow chart of the adaptive optimization process guided by the deep-learning methods.

caused by high-frequency structure, because although the low-frequency EM response of the meta-atom originates from the Jerusalem-cross resonator, surface currents are also induced on the small cross resonators (see Section S3 in the [Supplementary Material](#)). Here, we take x polarization as an example for demonstration and set the rotation angles of the metallic patterns as

0 deg. Figures 2(b) and 2(d) reveal changes in the simulated amplitude- and phase-frequency responses in dual-frequency bands with the stretch of different cross-shaped metallic patterns. As seen in Fig. 2(d), the propagation phase at low frequency obtains a coverage of near 360 deg, while that in high frequency does not change as l_{x1} varies. So, once the required

phase modulations of RCP and LCP in high frequency are confirmed, the high-frequency parameters can be directly designed according to Eqs. (1)–(3) and the mapping relationship between geometric/propagation phases and parameters [Fig. 2(f)]. However, in the high-frequency band, the change of l_{x2} influences both phases in the high frequency and low frequency at the same time [Fig. 2(e)]. Although the propagation phase can also cover 360 deg at high frequency, it also adds a cross talk of about 100 deg at low frequency. Such cross talk increases the difficulty of designing parameters for low-frequency operation. Moreover, the proposed dual-band spin-decoupled structure has considerable frequency and polarization cross talk; more details are shown in Section S4 in the [Supplementary Material](#).

To explore the relationship between the physical parameters of the meta-atom and the geometric/propagation phase in the two frequency bands, we divide the influence degree of parameters on the phase responses into four levels [(1) Hardly affect, (2) mildly affect, (3) severely affect, and (4) fundamentally affect; see Table S1 in Section S5 in the [Supplementary Material](#) for specific division indicators], and express it with a radar chart for an intuitional view, as shown in Fig. 2(g). The investigated parameters are l_{x1} , l_{y1} , α , l_{x2} , l_{y2} , and β , while the other physical parameters keep fixed. The geometric phase and propagation phase at high frequency are all determined by parameters (l_{x2} , l_{y2} , and β), but the phase responses at low frequency are determined by all six parameters (l_{x1} , l_{y1} , α , l_{x2} , l_{y2} , and β), which exactly corresponds to the six physical parameters (P_1 , P_2 , P_3 , P_4 , P_5 , and P_6) that need to be output in the proposed methodology in Fig. 1. Therefore, we first determine the high-frequency parameters according to the high-frequency phase modulation requirements. Then, we take this as the preset condition to obtain the adaptive optimization of low-frequency physical parameters according to the prior knowledge (see Section S6 in the [Supplementary Material](#)), and finally, satisfy the requirements for quad-channel wavefront tailoring. The overall schematic diagram of the inverse design of the meta-atom model is shown in the bottom-right panel of Fig. 1, including the classifier, ANN, and iteration process. Specifically, the classifier and ANN are applied to solve the cross talk of the propagation phase, and the iteration process is to cancel that of the geometric phase. Once we input the desired reflection phases of the four CP channels into the computer, the six physical parameters of the required meta-atom can be automatically output by the model. In fact, the cross talk faced by meta-atoms with different high-frequency physical parameters is also different. It will be difficult to use a unified neural network to predict the cross talk in all situations. Aiming at achieving the inverse design of the meta-atom more pertinently, we use a classifier to distinguish different phase modulation requirements. Specifically, the classifier is applied to distinguish which type of cross talk should be suppressed for the input data, and it is constructed by neural network with three hidden layers; each layer has 30 neurons (see Section S7 in the [Supplementary Material](#)).

Then, a series of pretrained ANN models are applied to fit the nonlinear functions between l_{x1} (l_{y1}) and the propagation phase under different cross-talk conditions. MLP is selected as the applied ANN model for its superiority in solving the problems of regression.⁵⁵ Thus l_{x1} (l_{y1}) can be predicted and output automatically on a millisecond time scale, instead of being obtained through tedious parameters sweeping and optimization in full-wave simulation. Therefore, the propagation phase and its corresponding l_{x1} (l_{y1}) are used as the input data and output

data in these ANN models, respectively. Specifically, the training process of ANN can be divided into three parts data gathering, data processing, and neural network optimization. First, the parameters for high frequency (l_{x2} , l_{y2} , and β) can be calculated and searched by Eqs. (1)–(3) and Fig. 2(f); then they need to be fixed while the parameters for low frequency varies. On this basis, a total of 3200 training samples were generated from full-wave simulation results. Second, we extract the relative phase at high frequency from each simulated spectrum and input them to the ANN model. Finally, by optimizing the number of neurons and hidden layers, learning rate, and so on, the {propagation phase} $\rightarrow l_{x1}$ (l_{y1}) mapping in different cross-talk situations can be established (see Section S7 in the [Supplementary Material](#)). The final optimized ANN model includes two hidden layers with 20 neurons and one output layer. The Adam optimizer was chosen to optimize the weight parameters due to its ability to improve the convergence speed. Training processes of both the classifier and ANN models are realized based on the Pytorch with version 1.1.0 and Anaconda platform with Python version 3.7.0. Learning rates of the classifier and ANN models are set as 0.01 and 0.001, respectively. The Adam optimizer is applied to the training process, and their accuracy can reach larger than 95% after being optimized via 190 and 110 epochs, respectively. More details about the training loss, accuracy, and error histogram are shown in Section S8 of the [Supplementary Material](#).

We use “ $\varphi_{f_2}^R/\varphi_{f_2}^L/\varphi_{f_1}^R/\varphi_{f_1}^L$ ” to describe the reflection phase for the RCP/LCP wave (denoted by the superscript of R or L) at low/high frequency (denoted by subscript of f_1 or f_2). A meta-atom is defined as the phase calibration reference with the parameters $\{l_{x1}, l_{y1}, \alpha, l_{x2}, l_{y2}, \beta\}$ being 8.50 mm, 5.03 mm, 0 deg, 4.50 mm, 3.91 mm, and 0 deg, respectively. As shown in Fig. 2(h), the deep-learning-guided adaptive optimization process here is to gradually adjust the physical parameters, aiming at reducing the phase error and gradually approaching the final target. We compare the EM performances of the meta-atoms output by the inverse design model with the design targets to evaluate the model. The threshold values, set as phase errors, are lower than 10 deg, and the amplitudes are all >0.9 . For example, we set the design target of phase modulations of “ $\varphi_{f_2}^R/\varphi_{f_2}^L/\varphi_{f_1}^R/\varphi_{f_1}^L$ ” as 0 deg/90 deg/180 deg/270 deg. If the four-channel phase modulations of the meta-atom output in this iteration is 2 deg/93 deg/178 deg/276 deg, all of the phase differences compared with the design targets are within 10 deg, and at the same time, if all the amplitudes in these four channels are above 0.9, we consider the model to meet the requirements at this time. Such parameter iterations only need about five epochs to output the structural parameters that meet the phase targets. For very few elements that still fail to meet the requirements after dozens of iterations (due to the propagation phase coverage slightly <360 deg), the amplitude and phase errors will be comprehensively evaluated and the physical parameters for the meta-atom with the closest EM responses to the target will be selected for output. The meta-atom with six initial parameters is simulated, and three of their low-frequency physical parameters are replaced if the target has not been reached. The substitution of $\{l_{x1'}, l_{y1'}, \alpha'\}$ for $\{l_{x1}, l_{y1}, \alpha\}$ is obtained with the support of the above-mentioned classifier, ANN, and the deformation of Eqs. (1)–(3) (see Sections S6 and S9 in the [Supplementary Material](#)).

As a design example, we consider a 2-bit coding metasurface for four CP channels, that is, the reflection phases of 0 deg, 90 deg, 180 deg, and 270 deg in each channel can be combined

arbitrarily. Since a 2-bit coding metasurface is usually sufficient for realizing a variety of EM functions, we consider a 2-bit coding metasurface as a design example to verify the proposed approach. In fact, the phase states are not limited to these four states (0 deg, 90 deg, 180 deg, 270 deg) and can be readily extended to other combinations, e.g., 3-bit (eight phase states in each channel) meta-atoms. For the proposed dual-spin/frequency multiplexing metasurface, a total of $4^4 = 256$ meta-atoms are required because each of the four channels possesses four phase states. As for the high-frequency resonators, they have $4^2 = 16$ kinds of configurations. When the high-frequency structure is determined, we can obtain a total of $16 \times 2 = 32$ (for x -LP and y -LP, respectively) kinds of propagation phase-length functions at low frequency, which can be actually reduced to 12 due to the symmetry of the structure (see Section S10 in the [Supplementary Material](#)). Finally, the parameters for constructing the 2-bit coding metasurface are determined by the proposed deep-learning-assisted method. It should be noted that all these steps are automatically executed by the inverse design method without human intervention. Some studies about the inverse design of metasurfaces relying only on deep-learning methods require manual intervention to minimize loss function and improve the prediction accuracy by tuning the parameters of the model when establishing the mapping between EM responses and structural parameters.^{46,67} Here, the proposed approach comprises a series of simple neural network models and a prior-knowledge-based iteration algorithm, for which the manual optimization process for the parameters of neural network models can be omitted. For example, if a meta-atom with $\varphi_{f_2}^R/\varphi_{f_2}^L/\varphi_{f_1}^R/\varphi_{f_1}^L = 0 \text{ deg}/90 \text{ deg}/270 \text{ deg}/180 \text{ deg}$ is required, we can directly obtain $l_{x2} = 4.19 \text{ mm}$, $l_{y2} = 3.82 \text{ mm}$, and $\beta = 22.5 \text{ deg}$ according to Eqs. (1)–(3) and Fig. 2(f). Then, these three parameters are used as the preset conditions of the adaptive optimization part in the methodology and the “270 deg/180 deg” in the low-frequency channels as the optimization target, and then the three low-frequency parameters as $l_{x1} = 8.5 \text{ mm}$, $l_{y1} = 4.89 \text{ mm}$, and $\alpha = 69.0 \text{ deg}$ will be output. Finally, 256 meta-atoms are automatically designed by this approach with desired phase modulation and high reflection efficiency in four channels (see Section S11 in the [Supplementary Material](#)).

Based on the above study, we further develop a top-to-bottom metasurface design method. As shown in Fig. 1, only the quad-channel phase distributions for versatile wave functionalities are input into a computer and then it can output all the parameters of desired meta-atoms automatically, avoiding the tedious process of the manual optimization for cross-talk suppression. Each meta-atom embedded in the metasurface can achieve the desired quad-channel phase response in minutes. Different from inverse design approaches based only on neural networks, the proposed method additionally combines physical theorems in EM waves, which has been proven an effective strategy to reduce the amount of training data and training time.⁶⁸

2.2 Dual-Frequency Metasurface for Independent Spin-to-OAM Conversion

To demonstrate the feasibility of the top-to-bottom metasurface design method, we first design a dual-frequency metasurface for quad-channel-independent spin-to-OAM conversion. Assuming that the independent spatial phase distribution of four CP channels at two frequencies is described by $\Phi_{f_2}^R$, $\Phi_{f_2}^L$, $\Phi_{f_1}^R$, and $\Phi_{f_1}^L$,

where the superscript and subscript represent the polarization channel and the frequency channel, respectively.

The functional diagram of this design example is shown in Fig. 1. The phase distributions are calculated by adding together the phase gradient in different directions to anomalously deflect the generated OAM vortices. The helical phase distribution for OAM generation can be calculated as

$$\Phi_l^{\text{OAM}}(x, y) = l \cdot \arctan(y/x) \quad \text{with } l = -2, -1, 1, \text{ and } 2, \quad (4)$$

where l is the topological charge and (x, y) is the coordinate position of the meta-atom. To much clearly distinguish the incident and reflected beams for real application, we added an additional phase gradient for each channel to deflect the generated OAM beam into an off-axis one. It should be noted that the topological charges and directions of off-axis OAM beams with different spin states generated by PB-phase-only metasurface are linked due to the spin coupling.^{19,69} But the limitation can be effectively breached by the spin-decoupled metasurface.²⁹ To verify the spin-decoupled property of the metasurface, the four independent wavefronts of off-axis vortex beams are designed and derived as

$$\Phi_{f_1}^R(x, y) = \Phi_{-1}^{\text{OAM}} + \frac{\pi}{4p}y, \quad (5)$$

$$\Phi_{f_1}^L(x, y) = \Phi_{-2}^{\text{OAM}} - \frac{\pi}{4p}x, \quad (6)$$

$$\Phi_{f_2}^R(x, y) = \Phi_{+2}^{\text{OAM}} - \frac{\pi}{2p}y, \quad (7)$$

$$\Phi_{f_2}^L(x, y) = \Phi_{+1}^{\text{OAM}} + \frac{\pi}{2p}x. \quad (8)$$

The detailed design process can be found in Section S12 in the [Supplementary Material](#). The inverse design approach can output the required physical parameters based on the input phase distribution $\Phi_{f_2}^R$, $\Phi_{f_2}^L$, $\Phi_{f_1}^R$, and $\Phi_{f_1}^L$. Figure 3(a) provides the output distributions of physical parameters of l_{x1} , l_{y1} , α , l_{x2} , l_{y2} , and β , and Fig. 3(b) displays the required discretized phase distributions in four channels. The OAM metagenerator composed of the meta-atoms with computer-output parameters is simulated in commercial software and fabricated through the standard printed circuit board (PCB) technique. The metasurface prototype [shown in Fig. 3(c)] has a radius of 205 mm and a thickness of 3.7 mm, containing about 1200 meta-atoms. The diameter of the prototype is about 13 and 24 times the wavelength for low frequency at 9.8 GHz and high frequency at 17.8 GHz, respectively. Figure 3(d) illustrates the simulated far-field power patterns of the generated OAM beams under the illumination of RCP and LCP waves at two frequencies. We denote elevation angle and azimuth angle as θ and φ , and express the beam direction in the form of (θ, φ) . Clearly, the directions of the four vortex beams (denoted as #1 to #4) are deflected to four different off-axis directions, which are (26 deg, 90 deg), (26 deg, 180 deg), (22 deg, -90 deg), and (22 deg, 0 deg), respectively. Besides, the prototype is also measured with a three-dimensional near-field scanning system.

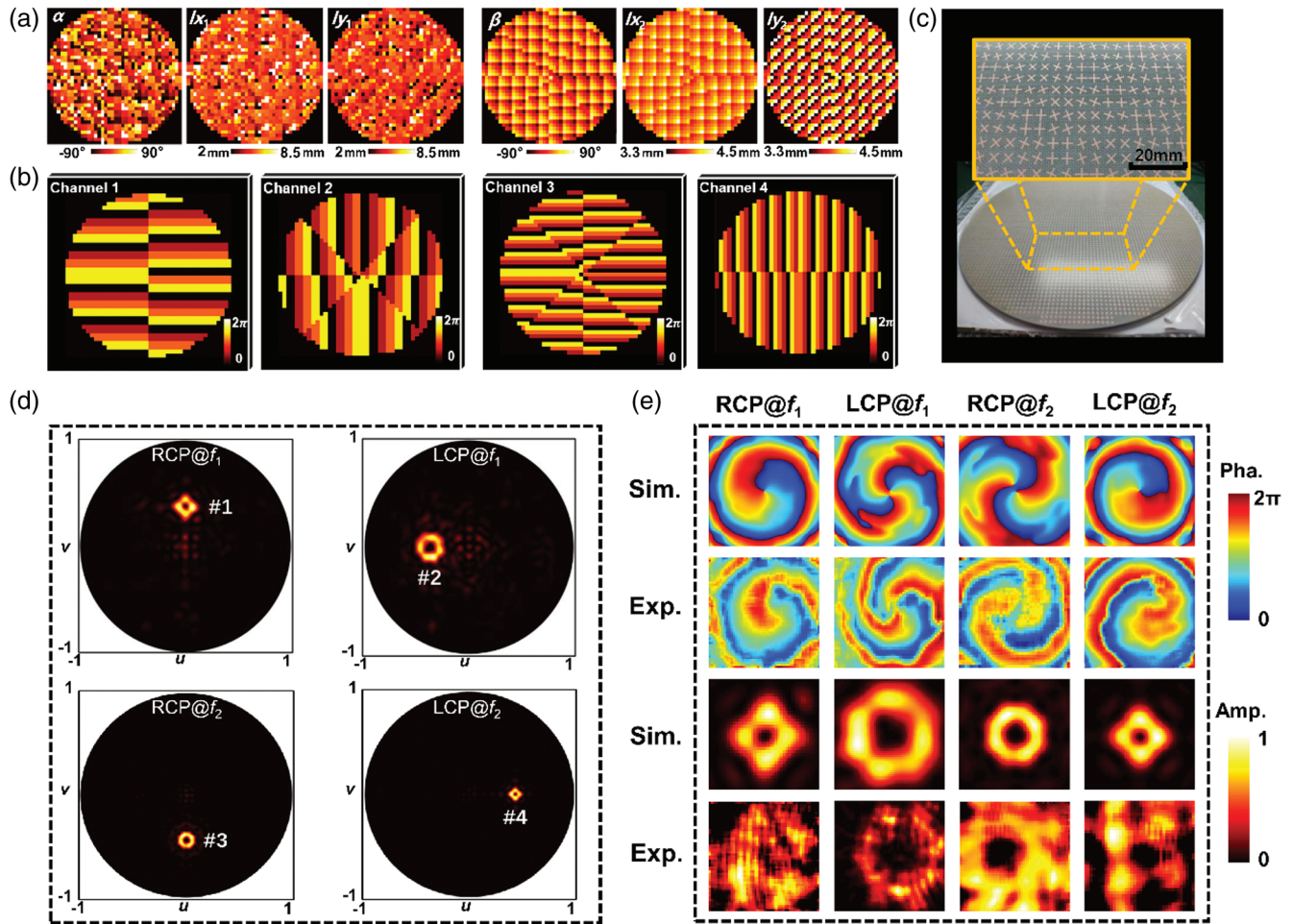


Fig. 3 Realization of dual-frequency spin-to-orbit metaconverter. (a) Physical parameter distributions of the elements in sample 1. (b) Calculated phase distribution for RCP channel at 9.8 GHz, LCP channel at 9.8 GHz, RCP channel at 17.8 GHz, and LCP channel at 17.8 GHz. (c) Photograph of the fabricated spin-to-orbit metaconverter. (d) Normalized simulated power patterns in momentum space. (e) Simulated and measured intensity patterns and phase patterns of different OAM beams in the four channels.

Figure 3(e) shows the simulated and measured amplitude and phase distributions at a distance of 1000 mm from the prototype. On the one hand, the measured amplitude distributions in four channels have obvious doughnut-like shapes with little energy in the center, thus forming the energy “singularity” – a fundamental feature of an OAM beam.^{70,71} On the other hand, with the increase of the absolute value of the topological charge, the radius of the intensity ring also increases gradually (by comparing #2 and #1, #3, and #4), which is also the typical characteristic of the vortex beam.² It should be noted that the intensity profiles of +1 and -1 in Fig. 3(e) exhibit a rectangular ring shape; this is because the helical phase of 360 deg at this time is discretized into four states, and the finite number of discrete phase states causes the minor difference of intensity distribution from the ideal one. More theoretical analysis can be found in Section S13 of the [Supplementary Material](#). The measured OAM modes carried by the vortex beams agree with that of simulated results, successfully demonstrating the inverse design of spin/frequency multiplexing metasurface for generation of quad-channel independent vortex beams.

2.3 Dual-Frequency VVB Metamultiplexer via Spin Decoupling

To further demonstrate the inverse design approach, a VVB metamultiplexer is considered as the second example. When vortex beams carrying OAM with opposite spin states propagate along the same beam direction, they will be coherently superposed to generate VVB, which can be described by high-order Poincaré spheres (HOPSs).^{19,72} RCP (carrying OAM mode m) and LCP (carrying OAM mode n) in the reflected field correspond to the north and south poles of a HOPS, and the wave function of the superposition of these two vortices with different spin states can be denoted as $\text{HOPS}_{m,n}$. Recently, several works have proposed a VVB metagenerator operating in millimeter waves,¹⁹ terahertz waves,^{29,73} and optical regimes.^{69,72,74} However, they operate in a single-frequency band, leaving the potential of spin-frequency-multiplex unexploited; moreover, most of them only generate a VVB beam with $m + n = 0$ ($\text{HOPS}_{l,-l}$) or several pairs of mode-coupling off-axis beams that are symmetric about the surface normal. This restricted combination of modes

or combination of beam directions is not conducive to the widespread adoption of such devices into applications, which can be effectively overcome by the spin-decoupled metasurface (see Section S14 in the [Supplementary Material](#) for more discussion). Aiming at showing the ability to break these restrictions, we orderly design a single off-axis beam (denoted as #1) in the low-frequency band and two mode-decoupled off-axis VVBs (denoted as #2 and #3) in the high-frequency band. The wave function of a single beam is $\text{HOPS}_{-2,2}$ ($|m-n|=4$) at 9.8 GHz, and the other two beams are $\text{HOPS}_{1,2}$ ($|m-n|=1$) and $\text{HOPS}_{-1,2}$ ($|m-n|=3$) at 17.8 GHz, respectively. Specifically, the phase distributions of the four CP channels are designed as

$$\Phi_{f_1}^R(x, y) = \Phi_{+2}^{\text{OAM}} + \frac{\pi}{4p}y, \quad (9)$$

$$\Phi_{f_1}^L(x, y) = \Phi_{-2}^{\text{OAM}} + \frac{\pi}{4p}y, \quad (10)$$

$$\Phi_{f_2}^R(x, y) = \arg \left[\exp \left(\Phi_{+1}^{\text{OAM}} + \frac{\pi}{2p}x \right) + \exp \left(\Phi_{-1}^{\text{OAM}} - \frac{\pi}{2p}x \right) \right], \quad (11)$$

$$\Phi_{f_2}^L(x, y) = \arg \left[\exp \left(\Phi_{+2}^{\text{OAM}} + \frac{\pi}{2p}x \right) + \exp \left(\Phi_{+2}^{\text{OAM}} - \frac{\pi}{2p}x \right) \right]. \quad (12)$$

Figures 4(a) and 4(b) show the discretized parameter distributions of the meta-atom array and phase distributions for the

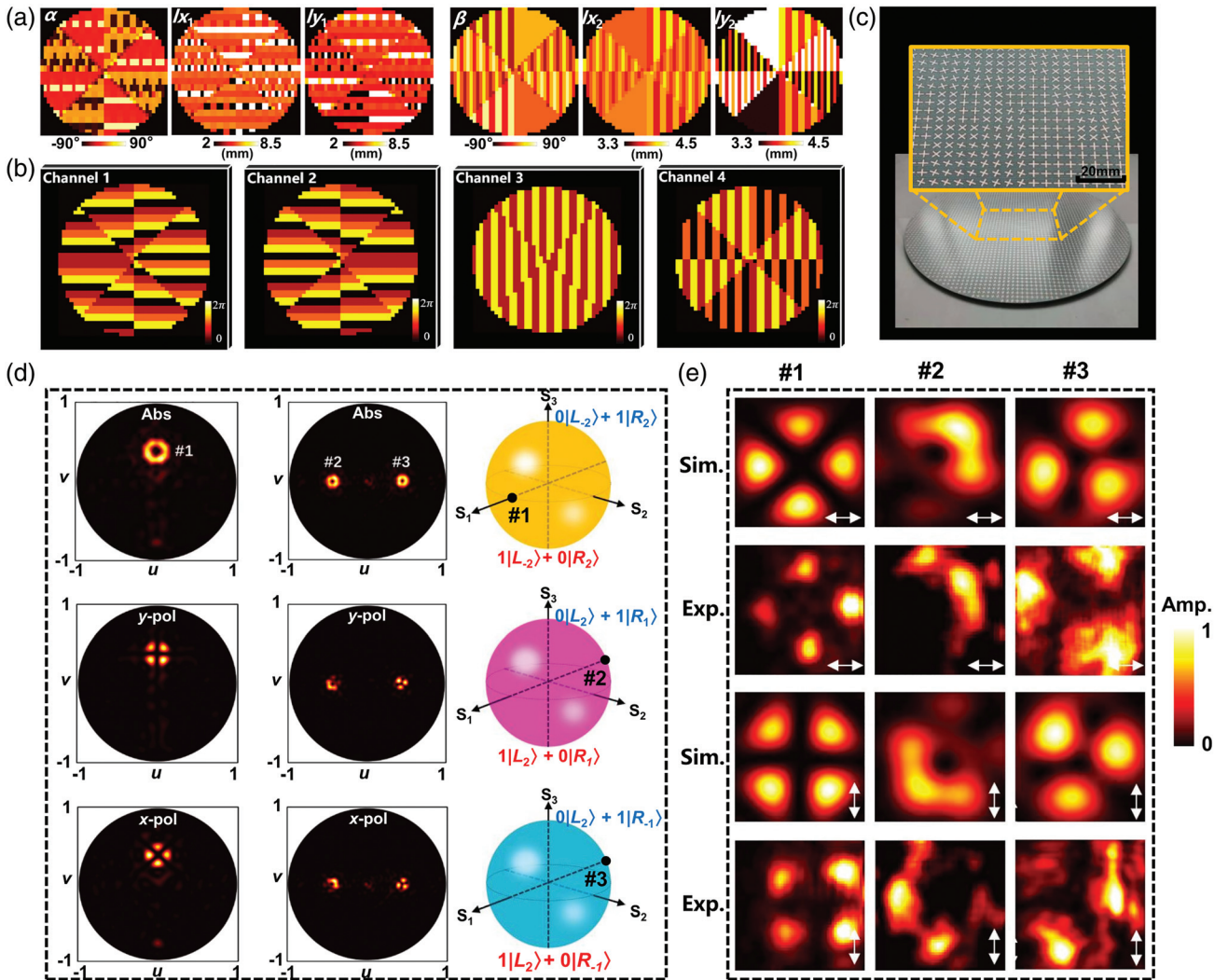


Fig. 4 Realization of dual-frequency VVB metamultiplexer. (a) Parameter distributions of the elements in sample 2. (b) Calculated phase distributions for RCP channel at 9.8 GHz, LCP channel at 9.8 GHz, RCP channel at 17.8 GHz, and LCP channel at 17.8 GHz. (c) Photograph of the fabricated VVB meta-multiplexer. (d) Normalized simulated power patterns and their positions on the three HOPSS. Beam #1 is designed at 9.8 GHz and beams #2 and #3 are designed at 17.8 GHz. (e) Simulated and measured intensity patterns of two orthogonal LP components. The white arrows indicate the detected polarization direction.

four CP channels, respectively. The prototype contains about 1100 meta-atoms, as displayed in Fig. 4(c). Figure 4(d) illustrates the reflected far-field power pattern under the normal illumination of an x -LP wave. As an LP wave can be decomposed into two orthogonal CP waves, we use an x -LP wave to shine the metasurface to equivalently provide LCP and RCP illuminations simultaneously. As for the spatial distribution of the reflected field, the single beam #1 is designed in the yo z plane, while beams #2 and #3 are in the xoz plane. Simulated results of the three HOPSs are shown in Fig. 4(d), as well as the positions of these three beams on the equator. Their longitude on the equator depends on the initial phase difference between RCP and LCP.¹⁹ The initial phase difference is 0 deg for #1 and 180 deg for #2 and #3. All of these generated beams (absolute far-field energy pattern) possess doughnut-like shape, verifying the typical characteristics of a vortex beam. The most principal feature of a VVB is its inhomogeneous polarization state along circumferential direction. To this end, we also analyze the output x -LP component and y -LP component of the reflected field. As shown in Fig. 4(e), the number of nulls in measured intensity pattern of these three VVBs are fully consistent with the designed value of $|m - n|$, and the two polarization components of the experimental results are in good agreement with the full-wave simulations. The nonuniform intensity distribution in the measured results is due to imperfections in the experiment setup and sample fabrication (see detailed discussion in Section S15 of the [Supplementary Material](#)).

The degree of freedom provided by the frequency and polarization channel can largely increase the information capacity of the metadvice. As another example, we also provide the design of a kaleidoscopic vortex generator that can generate 16-channel VBs or 8-channel HOPS beams (see Section S16 in the [Supplementary Material](#)). Besides, the realized vortex beams are not limited to that demonstrated herein. The inversely designed dual-spin/frequency metasurface that can generate OAM with other mode combinations ($l = 1, -2, 3, -4$ in four channels) is also shown in Section S17 in the [Supplementary Material](#). This method is also suitable for multiple vortex beams generation in the case of oblique incidence. We generate the same four vortex beams (shown in Fig. 3) under the illumination of a 24 deg oblique incident plane wave, which is shown in Section S18 in the [Supplementary Material](#). According to the above analysis and several design examples, the limitation of spin coupling has been broken in more than a single band. Moreover, the design difficulties caused by cross talk, which is tricky for manual optimization, can be effectively overcome by the deep-learning-assisted inverse design method.

3 Conclusion

We have proposed an inverse design method of dual-spin/frequency multiplexing metasurface. The deep-learning-assisted approach can solve the principal design difficulties due to the dual-frequency and polarization cross talk. The physical parameters of the metasurface can be automatically output by this methodology, once the desired phase responses in the four channels are input. As the design examples, frequency-multiplexing arbitrary spin-to-orbit conversion and dual-frequency off-axis VVB generation have been constructed and experimentally demonstrated. The inverse design method combining deep learning with prior knowledge may provide a route to rapidly solve complex EM problems in metasurface design. It possesses

a lower time cost compared with traditional optimization algorithms, and also can be extended to terahertz and optical regimes (see Section S19 in the [Supplementary Material](#) for more discussions). The approach also offers potentials for inverse design of reconfigurable metasurfaces, once active element parameters, such as liquid crystal⁷⁵ and diodes,⁵³ are also taken into account in the data set. The proposed method can also be extended to the optical region but maybe with some difficulties in the sample fabrication of multilayered metallic/dielectric structures and reduced efficiency due to the intrinsic material loss in the optical region. The combination of dual-spin/frequency OAM/VVB multiplexing, enhanced capacity, shared aperture, and compactness may render this methodology seductive for potential applications in quantum optics and wireless communication.

4 Appendix: Measurement

The frequency-multiplexing spin-to-orbit metaconverter and vector vortex metamultiplexer samples were fabricated by PCB technology and the performance was measured by a three-dimensional near-field scanning system in a standard microwave anechoic environment (see Section S20 in the [Supplementary Material](#)). When measuring the dual-band spin-to-orbit metaconverter, X-band and Ku-band CP horn antennas were used as the emitters. Four CP spiral antennas (respectively operating in two orthogonal CP modes in two frequency bands) were used as the near-field probe to record the amplitude and phase distribution in the scanning plane. For the vector vortex multiplexer sample, we used X-band and Ku-band LP horn antennas as the emitter and two LP dipole antennas as the near-field probe. In order to measure the field distribution of both the x -LP and y -LP EM fields, the dipole antennas are set to horizontal and vertical directions, respectively. In addition, rotating the samples allows us to measure the off-axis VBs and VVBs in different planes. The scanning area is 500 mm \times 500 mm, and the scanning step is set as 3 mm.

Acknowledgments

This work was supported by the National Natural Science Foundation of China (Grant Nos. 62271243 and 62071215), the National Key Research and Development Program of China (Grant No. 2017YFA0700201), the Joint Fund of Ministry of Education for Equipment Pre-research (Grant No. 8091B032112), the Priority Academic Program Development of Jiangsu Higher Education Institutions, the Fundamental Research Funds for the Central Universities, and Jiangsu Provincial Key Laboratory of Advanced Manipulating Technique of Electromagnetic Wave.

Code, Data, and Materials Availability

The data that support the plots within this paper and other findings of this study are available from the corresponding author upon reasonable request.

References

1. G. Milione et al., "Higher-order Poincaré sphere, Stokes parameters, and the angular momentum of light," *Phys. Rev. Lett.* **107**(5), 053601 (2011).
2. A. M. Yao and M. J. Padgett, "Orbital angular momentum: origins, behavior and applications," *Adv. Opt. Photonics* **3**(2), 161–204 (2011).

3. J. He et al., "Generation and evolution of the terahertz vortex beam," *Opt. Express* **21**(17), 20230–20239 (2013).
4. F. E. Mahmoudi and S. D. Walker, "4-Gbps uncompressed video transmission over a 60-GHz orbital angular momentum wireless channel," *IEEE Wireless Commun. Lett.* **2**(2), 223–226 (2013).
5. Y. Yan et al., "High-capacity millimetre-wave communications with orbital angular momentum multiplexing," *Nat. Commun.* **5**, 4876 (2014).
6. S. Chen et al., "Cylindrical vector beam multiplexer/demultiplexer using off-axis polarization control," *Light Sci. Appl.* **10**(1), 222 (2021).
7. H. Ren et al., "Metasurface orbital angular momentum holography," *Nat. Commun.* **10**(1), 2986 (2019).
8. Q. Xiao et al., "Orbital-angular-momentum-encrypted holography based on coding information metasurface," *Adv. Opt. Mater.* **9**(11), 2002155 (2021).
9. G. B. Xavier and G. Lima, "Quantum information processing with space-division multiplexing optical fibres," *Commun. Phys.* **3**(1), 9 (2020).
10. K. Huang et al., "Vector-vortex Bessel–Gauss beams and their tightly focusing properties," *Opt. Lett.* **36**(6), 888–890 (2011).
11. N. Bhebhe et al., "A vector holographic optical trap," *Sci. Rep.* **8**(1), 17387 (2018).
12. D. Haefner, S. Sukhov, and A. Dogariu, "Spin Hall effect of light in spherical geometry," *Phys. Rev. Lett.* **102**(12), 123903 (2009).
13. M. R. Akram et al., "Photon spin Hall effect-based ultra-thin transmissive metasurface for efficient generation of OAM waves," *IEEE Trans. Antennas Propag.* **67**(7), 4650–4658 (2019).
14. N. Shitrit et al., "Optical spin Hall effects in plasmonic chains," *Nano Lett.* **11**(5), 2038–2042 (2011).
15. Y. Liu et al., "Photonic spin hall effect in metasurfaces: a brief review," *Nanophotonics* **6**(1), 51–70 (2017).
16. P. J. Lavery Martin et al., "Detection of a spinning object using light's orbital angular momentum," *Science* **341**(6145), 537–540 (2013).
17. M. Zhao et al., "Measurement of the rotational Doppler frequency shift of a spinning object using a radio frequency orbital angular momentum beam," *Opt. Lett.* **41**(11), 2549–2552 (2016).
18. Y. Shen et al., "Optical vortices 30 years on: OAM manipulation from topological charge to multiple singularities," *Light Sci. Appl.* **8**(1), 90 (2019).
19. Z. H. Jiang et al., "A single noninterleaved metasurface for high-capacity and flexible mode multiplexing of higher-order Poincaré sphere beams," *Adv. Mater.* **32**(6), 1903983 (2020).
20. K. Zhang et al., "A review of orbital angular momentum vortex beams generation: from traditional methods to metasurfaces," *Appl. Sci.* **10**(3), 1015 (2020).
21. K. Chen et al., "Directional Janus metasurface," *Adv. Mater.* **32**(2), 1906352 (2020).
22. K. Chen et al., "A reconfigurable active Huygens' metalens," *Adv. Mater.* **29**(17), 1606422 (2017).
23. S. B. Glybovski et al., "Metasurfaces: from microwaves to visible," *Phys. Rep.* **634**, 1–72 (2016).
24. R. C. Devlin et al., "Arbitrary spin-to-orbital angular momentum conversion of light," *Science* **358**(6365), 896 (2017).
25. N. Yu et al., "Light propagation with phase discontinuities: generalized laws of reflection and refraction," *Science* **334**(6054), 333 (2011).
26. S. Pancharatnam, "Generalized theory of interference, and its applications," *Proc. Indian Acad. Sci. – Sect. A* **44**(5), 247–262 (1956).
27. M. V. Berry, "The adiabatic phase and Pancharatnam's phase for polarized light," *J. Mod. Opt.* **34**(11), 1401–1407 (1987).
28. G. Ding et al., "Dual-helicity decoupled coding metasurface for independent spin-to-orbital angular momentum conversion," *Phys. Rev. Appl.* **11**(4), 044043 (2019).
29. Y. Xu et al., "Generation of terahertz vector beams using dielectric metasurfaces via spin-decoupled phase control," *Nanophotonics* **9**(10), 3393–3402 (2020).
30. J. Shabanpour, "Programmable anisotropic digital metasurface for independent manipulation of dual-polarized THz waves based on a voltage-controlled phase transition of VO₂ microwires," *J. Mater. Chem. C* **8**(21), 7189–7199 (2020).
31. Q. Hu et al., "Arbitrary and dynamic Poincaré sphere polarization converter with a time-varying metasurface," *Adv. Opt. Mater.* **10**(4), 2101915 (2022).
32. J. P. Balthasar Mueller et al., "Metasurface polarization optics: independent phase control of arbitrary orthogonal states of polarization," *Phys. Rev. Lett.* **118**(11), 113901 (2017).
33. Y. Yuan et al., "Complementary transmissive ultra-thin meta-deflectors for broadband polarization-independent refractions in the microwave region," *Photonics Res.* **7**(1), 80–88 (2019).
34. H.-X. Xu et al., "Completely spin-decoupled dual-phase hybrid metasurfaces for arbitrary wavefront control," *ACS Photonics* **6**(1), 211–220 (2019).
35. H.-X. Xu et al., "Multiplexed metasurfaces: wavevector and frequency multiplexing performed by a spin-decoupled multichannel metasurface," *Adv. Mater. Technol.* **5**(1), 2070005 (2020).
36. O. Khatib et al., "Deep learning the electromagnetic properties of metamaterials—a comprehensive review," *Adv. Funct. Mater.* **31**(31), 2101748 (2021).
37. M. M. R. Elsayy et al., "Numerical optimization methods for metasurfaces," *Laser Photonics Rev.* **14**(10), 1900445 (2020).
38. W. Ma et al., "Deep learning for the design of photonic structures," *Nat. Photonics* **15**(2), 77–90 (2021).
39. S. Molesky et al., "Inverse design in nanophotonics," *Nat. Photonics* **12**(11), 659–670 (2018).
40. W. Ma, F. Cheng, and Y. Liu, "Deep-learning-enabled on-demand design of chiral metamaterials," *ACS Nano* **12**(6), 6326–6334 (2018).
41. J. Peurifoy et al., "Nanophotonic particle simulation and inverse design using artificial neural networks," *Sci. Adv.* **4**(6), eaar4206 (2018).
42. Q. Zhang et al., "Machine-learning designs of anisotropic digital coding metasurfaces," *Adv. Theor. Simul.* **2**(2), 1800132 (2018).
43. S. An et al., "A deep learning approach for objective-driven all-dielectric metasurface design," *ACS Photonics* **6**(12), 3196–3207 (2019).
44. L. Gao et al., "A bidirectional deep neural network for accurate silicon color design," *Adv. Mater.* **31**(51), 1905467 (2019).
45. H. P. Wang et al., "Deep learning designs of anisotropic metasurfaces in ultrawideband based on generative adversarial networks," *Adv. Intell. Syst.* **2**(9), 2000068 (2020).
46. R. Zhu et al., "Phase-to-pattern inverse design paradigm for fast realization of functional metasurfaces via transfer learning," *Nat. Commun.* **12**(1), 2974 (2021).
47. C. C. Nadell et al., "Deep learning for accelerated all-dielectric metasurface design," *Opt. Express* **27**(20), 27523–27535 (2019).
48. T. Shan et al., "Coding programmable metasurfaces based on deep learning techniques," *IEEE J. Emerg. Sel. Top. Circuits Syst.* **10**(1), 114–125 (2020).
49. F. Ghorbani et al., "Deep neural network-based automatic metasurface design with a wide frequency range," *Sci. Rep.* **11**(1), 7102 (2021).
50. F. Ghorbani et al., "A deep learning approach for inverse design of the metasurface for dual-polarized waves," *Appl. Phys. A* **127**(11), 869 (2021).
51. R. Zhu et al., "Multiplexing the aperture of a metasurface: inverse design via deep-learning-forward genetic algorithm," *J. Phys. D: Appl. Phys.* **53**(45), 455002 (2020).
52. L. Li et al., "Machine-learning reprogrammable metasurface imager," *Nat. Commun.* **10**(1), 1082 (2019).
53. C. Qian et al., "Deep-learning-enabled self-adaptive microwave cloak without human intervention," *Nat. Photonics* **14**(6), 383–390 (2020).
54. C. Liu et al., "A programmable diffractive deep neural network based on a digital-coding metasurface array," *Nat. Electron.* **5**(2), 113–122 (2022).

55. T. Qiu et al., "Deep learning: a rapid and efficient route to automatic metasurface design," *Adv. Sci.* **6**(12), 1900128 (2019).
56. H. Taghvaei et al., "Radiation pattern prediction for metasurfaces: a neural network-based approach," *Sensors* **21**(8), 2765 (2021).
57. A. Mall et al., "Fast design of plasmonic metasurfaces enabled by deep learning," *J. Phys. D: Appl. Phys.* **53**(49), 49LT01 (2020).
58. M. Diligenti, S. Roychowdhury, and M. Gori, "Integrating prior knowledge into deep learning," in *16th IEEE Int. Conf. Mach. Learn. and Appl. (ICMLA)*, 18–21 December, pp. 920–923 (2017).
59. S. Chakraborty et al., "Incorporation of prior knowledge in neural network model for continuous cooling of steel using genetic algorithm," *Appl. Soft Comput.* **58**, 297–306 (2017).
60. S. Chen, Y. Leng, and S. Labi, "A deep learning algorithm for simulating autonomous driving considering prior knowledge and temporal information," *Comput.-Aided Civ. Infrastruct. Eng.* **35**(4), 305–321 (2020).
61. M. Yannai et al., "Spectrally interleaved topologies using geometric phase metasurfaces," *Opt. Express* **26**(23), 31031–31038 (2018).
62. L. Yan et al., "0.2 λ_0 thick adaptive retroreflector made of spin-locked metasurface," *Adv. Mater.* **30**(39), 1802721 (2018).
63. W. Yang et al., "Angular-adaptive reconfigurable spin-locked metasurface retroreflector," *Adv. Sci.* **8**(21), 2100885 (2021).
64. P. Xu et al., "Dual-circularly polarized spin-decoupled reflectarray with FSS-back for independent operating at Ku-/Ka-bands," *IEEE Trans. Antennas Propag.* **69**(10), 7041–7046 (2021).
65. T. Yue, Z. H. Jiang, and D. H. Werner, "A compact metasurface-enabled dual-band dual-circularly polarized antenna loaded with complementary split ring resonators," *IEEE Trans. Antennas Propag.* **67**(2), 794–803 (2019).
66. X. Tong et al., "Dual-wideband dual-circularly-polarized shared-aperture reflectarrays with a single functional substrate for K-/Ka-band applications," *IEEE Trans. Antennas Propag.* **70**(7), 5404–5417 (2022).
67. X. Han et al., "Inverse design of metasurface optical filters using deep neural network with high degrees of freedom," *InfoMat* **3**(4), 432–442 (2021).
68. P. Liu, L. Chen, and Z. N. Chen, "Prior-knowledge-guided deep-learning-enabled synthesis for broadband and large phase-shift range metacells in metalens antenna," *IEEE Trans. Antennas Propag.* **70**(7), 5024–5034 (2022).
69. F. Yue et al., "Multichannel polarization-controllable superpositions of orbital angular momentum states," *Adv. Mater.* **29**(15), 1603838 (2017).
70. L. Allen et al., "Orbital angular momentum of light and the transformation of Laguerre-Gaussian laser modes," *Phys. Rev. A* **45**(11), 8185–8189 (1992).
71. A. T. O'Neil et al., "Intrinsic and extrinsic nature of the orbital angular momentum of a light beam," *Phys. Rev. Lett.* **88**(5), 053601 (2002).
72. Y. Bao, J. Ni, and C.-W. Qiu, "A minimalist single-layer metasurface for arbitrary and full control of vector vortex beams," *Adv. Mater.* **32**(6), 1905659 (2020).
73. C. Zheng et al., "All-dielectric metasurface for manipulating the superpositions of orbital angular momentum via spin-decoupling," *Adv. Opt. Mater.* **9**(10), 2002007 (2021).
74. M. Liu et al., "Broadband generation of perfect Poincaré beams via dielectric spin-multiplexed metasurface," *Nat. Commun.* **12**(1), 2230 (2021).
75. J. Shabanpour et al., "Real-time multi-functional near-infrared wave manipulation with a 3-bit liquid crystal based coding metasurface," *Opt. Express* **29**(10), 14525–14535 (2021).

Kai Qu received his BE degree in optical engineering from the Harbin Institute of Technology, Harbin, China, in 2019. He is currently pursuing a PhD in electronic science and engineering at Nanjing University,

Nanjing, China. His current research focuses on the inverse design of multifunctional metasurfaces.

Ke Chen received his BS and PhD degrees in electronic science and engineering from Nanjing University, Nanjing, China, in 2012 and 2017, respectively. He is currently an associate professor at the Department of Electronic Engineering, School of Electronic Science and Engineering, Nanjing University. His research interests include electromagnetic metamaterials and metasurfaces and their applications to wireless communication and photonic devices. He received the Best Excellent Doctoral Dissertation Award of China Education Society of Electronics in 2018, Young Scientist Award of URSI General Assembly and Scientific Symposium (GASS) in 2021, and Young Scientist Award of International Applied Computational Electromagnetics Society (ACES) in 2021. He has hosted more than 10 research projects, such as the National Science Foundation of China and the Joint Fund of Ministry of Education for Equipment Pre-research. He has authored or co-authored over 70 peer-reviewed journal articles and over 60 refereed international conference papers.

Qi Hu received her BE degree in communication engineering from the Communication University of China, Beijing, China, in 2019. She is currently pursuing her PhD in electronic science and engineering at Nanjing University, Nanjing, China. Her current research focuses on metasurfaces.

Junming Zhao received his BS and PhD degrees in electronic science and engineering from Nanjing University, Nanjing, China, in 2003 and 2009, respectively. Since 2009, he has been a faculty member at the Department of Electronic Engineering, School of Electronic Science and Engineering, Nanjing University, where he is currently a professor. From January 2014 to January 2015, he was a visiting scholar with the Group of Antennas and Electromagnetics, School of Electronic Engineering and Computer Science, Queen Mary College, University of London. His research interests include electromagnetic metamaterials and metasurfaces and their applications to novel microwave functional devices.

Tian Jiang received his MSc and PhD degrees from the Department of Electronic Science and Engineering, Nanjing University, Nanjing, China, in 2004 and 2007, respectively. Since 2007, he has been a faculty member and currently, a professor at the Department of Electronic Engineering, School of Electronic Science and Engineering, Nanjing University. His research interests include electromagnetic metasurfaces and their application to microwave and photonic devices.

Yijun Feng received his PhD from the Department of Electronic Science and Engineering, Nanjing University, in 1992. Since then, he has been a faculty member and is currently a full professor and deputy dean of the School of Electronic Science and Engineering, Nanjing University. From September 1995 to July 1996, he was a visiting scientist at the physics department of Technical University of Denmark. From August 2001 to August 2002, he was a visiting researcher at the University of California, Berkeley. His research interests include electromagnetic metamaterials and their application to microwave and photonic devices, electromagnetic wave theory, and novel microwave functional materials. He has conducted more than 20 scientific research projects, including National 973, 863 Projects, National Natural Science Foundation projects, and the National Key Research and Development Program in China. He has served as the General Co-Chair of 2018 IEEE International Workshop on Antenna Technology, and Technical Program Co-Chair of 2013 International Symposium on Antennas and Propagation. He has received the 2010 Science and Technology Award (first grade) of Jiangsu Province, and the 2021 Science and Technology Award (first grade) of Shanxi Province, China. He has authored or co-authored over 200 peer-reviewed journal papers and over 160 refereed international conference papers.